Tuning the Dimensionality of Excitons in Colloidal Quantum Dot Molecules

James Cassidy,[1] Mingrui Yang,[1] Dulanjan Harankahage,[1] Dmitry Porotnikov,[1] Pavel Moroz,[1] Natalia Razgoniaeva,[1] Cole Ellison, [1,] Jacob Bettinger,[1] Shafqat Ehsan,[2] John Sanchez,[2] Jessica Madry,[3] Dmitriy Khon,[2] Mikhail Zamkov[1,]*

The Center for Photochemical Sciences and Department of Physics, Bowling Green State University, Bowling Green, Ohio 43403.[1] Department of Chemistry and Biochemistry, St. Mary's University, San Antonio, TX, 78228.[2] Texas A&M University College of Medicine, Bryan, TX 77807.[3]

Corresponding author: zamkovm@bgsu.edu; Tel: 419-372-0264; Fax: 419-372-9938

Abstract. Electrically-coupled quantum dots (QDs) can support unique optoelectronic properties arising from the superposition of single-particle excited states. Experimental methods for integrating colloidal QDs within the same nano-object, however, have remained elusive to the rational design. Here, we demonstrate a chemical strategy that allows assembling colloidal QDs into coupled composites, where proximal interactions give rise to unique optoelectronic behavior. The assembly method employing "adhesive" surfactants was used to fabricate both homogenous (e.g. CdS-CdS, PbS-PbS, CdSe-CdSe) and heterogeneous (e.g. PbS-CdS, CdS-CdSe) nanoparticle assemblies, exhibiting quasi-one-dimensional exciton fine structure. In addition, tunable mixing of single-particle exciton states was achieved for dimer-like assemblies of CdSe/CdS core-shell nanocrystals. The nanoparticle assembly mechanism was explained within the viscoelastic interaction theory adapted for molten-surface colloids. We expect that

the present work will provide the synthetic and theoretical foundation needed for building assemblies of many inorganic nanocrystals.

Keywords: biexcitons; qubits; g-CQD; single-particle; nanocrystals.

Multi-component nanostructures represents an emerging paradigm in colloidal nanoparticle research, which parallels the concept of supramolecular chemistry.[1] The ability to couple colloidal nanoparticles gives rise to interconnected systems, where multi-step energy conversion processes proceed with minimal energy and charge transfer distances.[2,3] Meanwhile, energetic communications between neighboring domains in such assemblies provide a feasible platform for developing hybrid systems with potential applications in photocatalysis,[4] biosensing,[5] quantum computing,[6] and multiexciton generation.[7]

To date, several methods have been explored towards fabricating multi-component colloidal nanocrystals (NCs). One is the seeded growth of one material domain onto the surface of another. This approach has yielded a variety of heterostructured morphologies, including core/shell,[8-10] Janus,[11,12] dot-in-a-rod,[13,14] barbell,[15-17] and more complex[18,19] nanostructures, where domain coupling enabled unique collective properties.[20-24] One of the limitations of this approach was a narrow range of material combinations and geometries achievable through a seeded-growth strategy. Chemical assembly techniques have helped alleviating these issues by employing molecular linkers to couple arbitrary colloidal nanoparticles.[25-29] The use of molecular conjugation, however, often led to a limited interaction between subunits, caused by steric conditions of bulky linkers. As a result, a collective behavior between incorporated components was often suppressed.[30-32] In addition to molecular conjugation methods, other strategies have also been developed for the assembly of colloidal nanocomposites. These included multiple precipitations to induced aggregation[33] and oriented attachment.[34] More recently, Banin et al.[35-38] has demonstrated a conceptually novel strategy for the assembly of colloidal nanocrystal molecules, which relied on using large colloidal beads as sites for inter-particle bonding. This approach has enabled the synthesis of CdSe/CdS core-shell dimers exhibiting inter-particle electronic interactions.

Here, we demonstrate colloidally-stable assemblies of semiconductor nanocrystals that support electronic communications across incorporated sites. The solution-phase assembly of colloidal nanocrystals was achieved through surfactant-directed surface interactions, which promoted the adhesion of nanoparticles at hybrid interfaces (Figure 1). This technique was demonstrated through the synthesis of

both homogenous assemblies of the same-type colloids (e.g. CdS-CdS, PbS-PbS, CdSe-CdSe), as well as heterogeneous assemblies of dissimilar nanocrystals (e.g. PbS-CdS, CdS-CdSe). Individual components of fabricated assemblies were found to engage in charge and energy transfer interactions across heterostructured interfaces. In particular, we observed that dimers of CdSe/CdS core/shell NC exhibited unique optical characteristics arising from a superposition of single-particle excitonic states. From the fabrication standpoint, the degree of inter-particle bonding at interfaces was tunable by changing the depth of the molten surface layer in original nanoparticles, as illustrated in Figure 1. The demonstrated assembly approach was explained within the viscoelastic interaction theory, which was adapted to account for molten surfaces in heated colloidal nanoparticles.

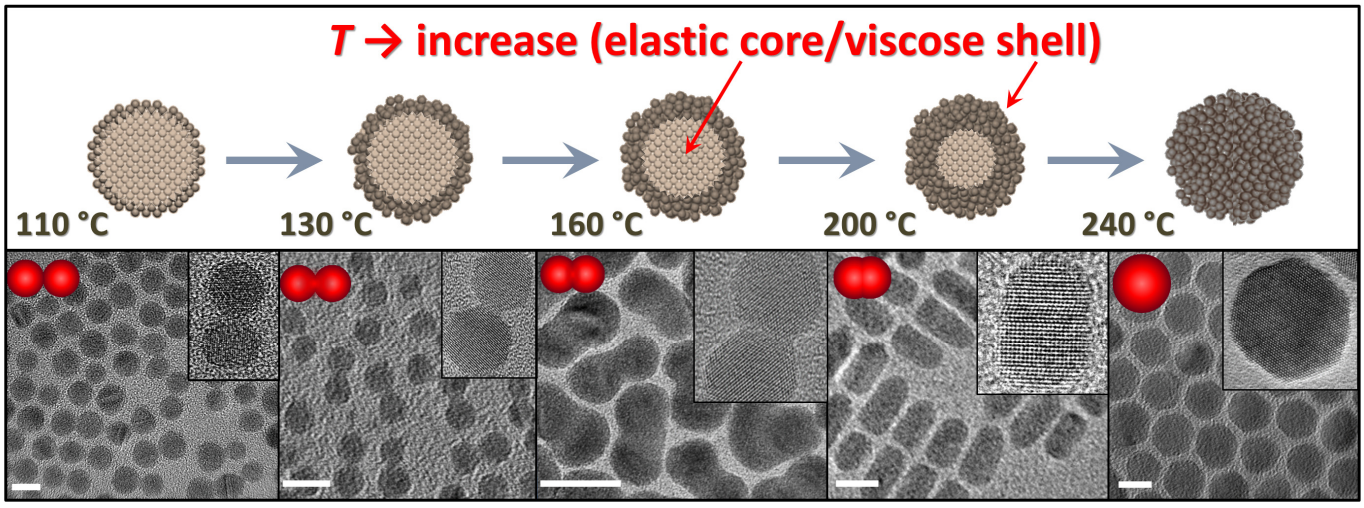

Figure 1. Illustration of the viscoelastic assembly approach. Formation of a molten layer in heated colloidal NCs enables bonding of nanoparticles at hybrid interfaces. The driving force for the assembly process is controlled by nanoparticle surfactants, while the degree of inter-particle fusion is tunable via the solvent temperature.

Results and discussion.

The intrinsic property of heated inorganic nanoparticles to form a molten surface layer was first demonstrated by works of Samorjai,[39] El-Sayed,[40] and Boret [41] on metal colloids. These studies have demonstrated that heated NCs of Au, Pt, and Pd formed a few-atom-deep liquid layer around the still solid core. The melting point of the surface was substantially lower than that of the bulk material due to a reduced surface tension of the solid-liquid interface. A similar melting point depression was observed for semiconductor NCs heated to 400 °C in vacuum.[42] More recently, solution-phase semiconductor

nanocrystals were also shown to undergo a similar solid-to-liquid transition at temperatures that were much lower than the corresponding bulk melting point (see Figure. S1).[43,44]

In the present work, the formation of molten surfaces in colloidal NCs helped achieving a partial fusion of nanoparticles in form of n-mer assemblies (Figure 1). The fusion of colloidal NCs required a proper balance between (1) - aggregative forces driving the particle attachment,[43] and (2) - opposing elastic forces,[45] associated with the elastic repulsion of solid "cores". Thermodynamically, the fusion of colloidal nanoparticles is driven by the reduction of the total surface area, A(ε), where $\varepsilon = \Delta L/L$ is a geometric strain coordinate (L is the size of uncompressed nanoparticles and ΔL is the compression distance – see Figure S2). The corresponding decrease in the interfacial energy, $E_{interfacial} = \gamma A(\varepsilon)$, is plotted in Figure 2a, where γ is the solvent/surfactant interfacial tension. These aggregative forces are counter-balanced by the increasing elastic energy, $E_{elastic}$ (Figure 2c), which represents the elastic repulsion of the two fusing nanoparticles due to the deformation of the lattice, $E_{elastic} = \frac{3}{2} G\varepsilon^2 V$, where $G(T)$ is the temperature-dependent nanoparticle shear modulus that characterizes the nanocrystal rigidity, and V is total volume of the coalescing nanostructures. The total free energy of the two fusing particles is thus given as a sum of the decreasing interfacial energy and increasing elastic energy terms:

$$E_{tot} = E_{interfacial} + E_{elastic} = \gamma \times A(\varepsilon) + \frac{3}{2} G(T)\, \varepsilon^2 V \quad (1)$$

Therefore, the coalescence of two particles is expected to stop at an particular stage corresponding to the minimization of the total energy, $E_{tot}(\varepsilon) \rightarrow \min$, for a given T (Figure 2b).

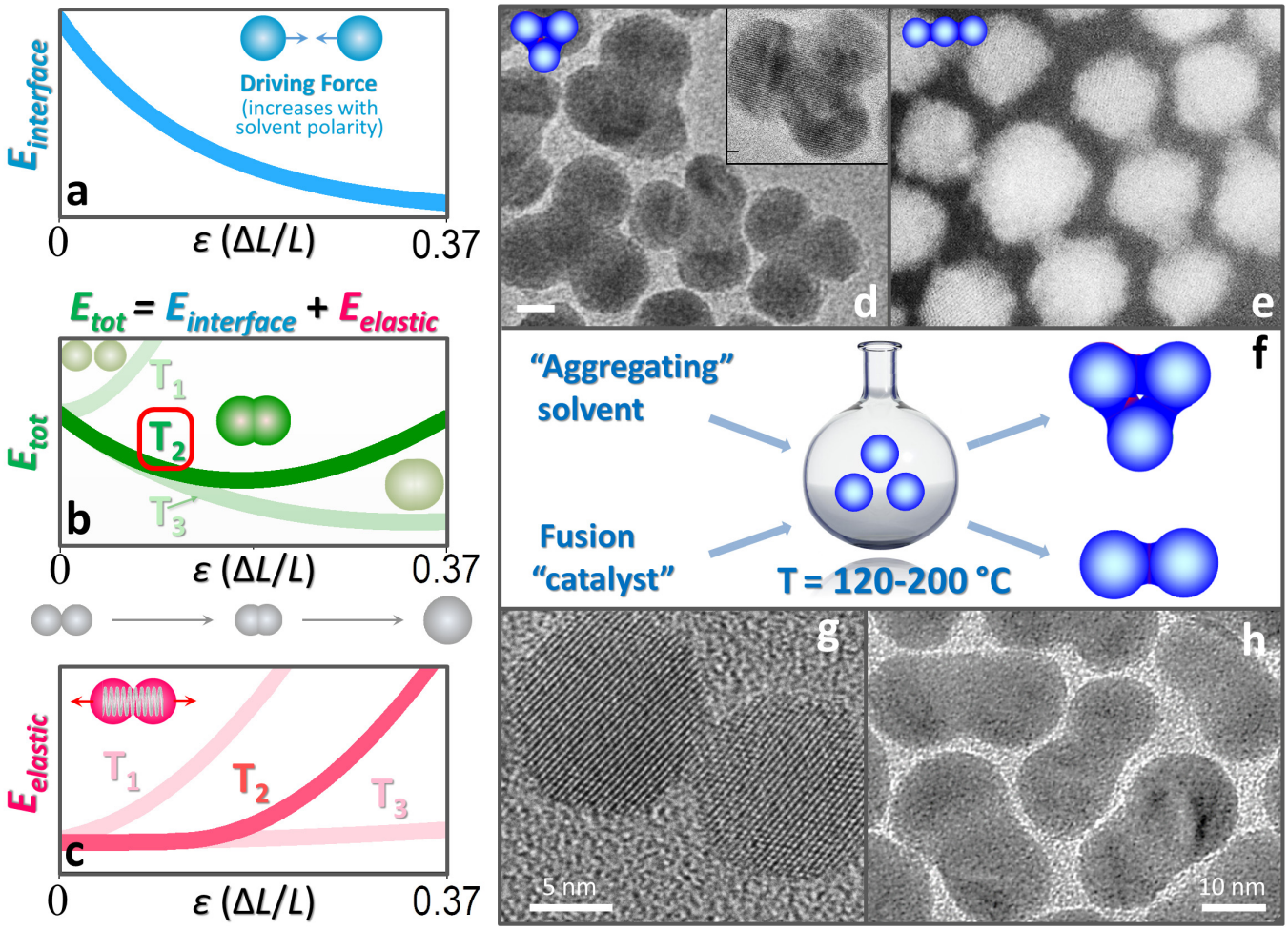

Figure 2. (a). Driving force towards particle aggregation caused by the reduction of the interfacial energy ($E_{interface}$) of fusing nanoparticles, which minimizes the total particle/solvent interfacial area. ε is the geometric strain coordinate $\varepsilon = \Delta L/L$ (L is the size of uncompressed nanoparticles and ΔL is the compression distance – see Figure S2). (b). Changes in the total free energy of fusing nanoparticles (E_{tot}), contributed by the reduction of the interfacial energy ($E_{interface}$) and the increase in the strain energy of elastic NCs ($E_{elastic}$), for three representative solvent temperatures, $T_1 < T_2 < T_3$. (c). The elastic energy of fusing nanoparticles ($E_{elastic}$), which represents their elastic repulsion that decreases with growing temperatures ($T_1 \rightarrow T_2 \rightarrow T_3$) due to melting. (d,e). Three-particle clusters of CdS nanocrystals, assembled at T = 180 °C and T = 120 °C, respectively. (f). Illustration of the assembly strategy, which involves the use of aggregation-inducing solvents and elemental chalcogenides to promote fusion of molten-surface nanoparticles. (g,h). Coupled dimers of CdS (g) and CdSe/CdS (h) nanocrystals, assembled at T = 120 °C and T = 200 °C, respectively.

According to Eq. 1, the degree of nanocrystal fusion (expressed as a function of compression strain – ε, see Figure S2) could be controlled by tuning either $E_{interface}$ (ε) or $E_{elastic}$ (ε) energy terms. For instance, increasing the difference between respective polarities of the solvent and the particle surfactant enhances

the driving force for particle aggregation, $dE_{interface}$ (ε)/dε. Meanwhile, increasing the solvent temperature causes a greater fraction of the surface layer, δ(T), to become molten (viscose), thus reducing $E_{elastic}$ within this layer, as illustrated in Figure 2c.

The fusion of colloidal nanocrystals is impeded by the stearic hindrance of long-chain amines or carboxylates present on particle surfaces. To overcome such a repulsion, we have employed two strategies that decrease the density of bulky ligands. The ***first*** method (schematically shown in Figure 2f) involved the exchange of long-chain ligands, such as oleic acid (OA) or oleylamine (OLAM), with small, atomic chalcogenides of the same type[46] (L → L, X → X). Figure S3 demonstrates that elemental S and Se behaved as L-type ligands, triggering a fast OLAM→(S, Se) exchange and simultaneous fusion of OLAM-deprived NCs. The decrease in the density of OLAM ligands following the addition of elemental chalcogenides was evident from the characteristic reduction of the inter-particle spacing in NC assemblies on a TEM grid, as illustrated in Figure SF3e. For OA-capped nanoparticles (X-type ligands), an efficient ligand exchange was achieved by using X-type anionic ligands in methanol (e.g. Na_2S), which injection promoted nanoparticle fusion (Figure SF4). The ***second*** strategy to overcome the compression strain of bulky ligands involved stripping the long-chain molecules. To this end, nanocrystals were transferred into a formamide (FA) solution via the OA → S^{2-} exchange (X-type to X-type) and heated to 110-150 °C, as detailed in the Sec. SI.2. Figures 2g and SF5a show examples of CdS NC molecules assembled using the FA heat-up strategy.

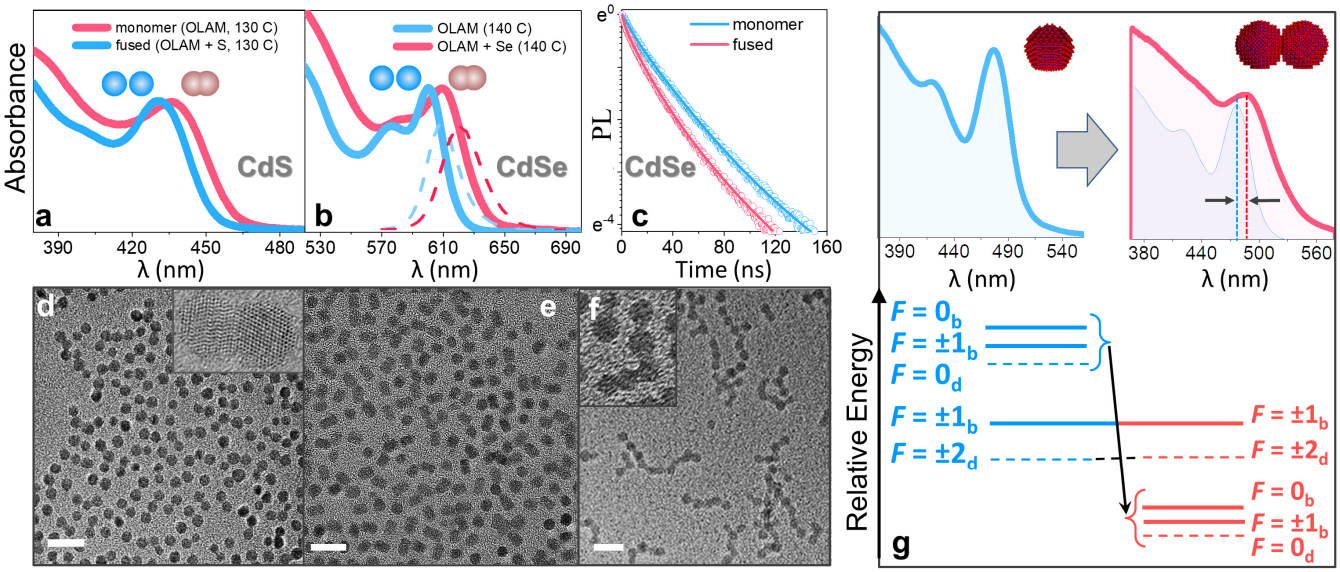

Figure 3. (a). Absorption profiles of isolated (blue) and fused (red) $CdS_{425\text{-nm}}$ NCs. (c). Emission and absorption profiles of isolated (blue) and fused (red) $CdSe_{600\text{-nm}}$ NCs (d,f). (c). PL intensity decay of

isolated (blue) and fused (red) $CdSe_{600\text{-}nm}$ NCs. (d). TEM images of fused $CdS_{425\text{-}nm}$ NCs. Scale bar = 15 nm. (e). TEM images of fused $CdSe_{600\text{-}nm}$ NCs. Scale bar = 15 nm. (f). TEM images of fused $CdS_{425\text{-}nm}$ NCs. Scale bar = 20 nm. (g). Experimental absorption spectra for isolated (blue) and fused (red) $CdSe_{480\text{-}nm}$ NCs along with predicted exciton fine structure changes for wurtzite CdSe NCs occurring during a transition from a dot (blue) to a rod (red) morphology.[47] *F* is the total angular momentum of an excitonic state (b = bright, d = dark)

Figures 3d and 3e show two examples of homogenous assemblies obtained by injecting elemental chalcogenides into an OLAM solution of colloidal NCs. The polar head group (HN_2, CO_2H) of unattached OLAM molecules renders the solution more polar compared to alkyl-terminated colloidal nanoparticles, providing the necessary driving force for particle aggregation.[48] The assembly of (n)-CdS and (n)-CdSe NC clusters was achieved by the injection of sulfur and selenium, respectively. For both NC types, TEM images (Figures 3d and 3e) show the formation of fused structured. A slight higher temperature used for CdSe NCs has resulted in a greater degree of fusion at interfaces. The concentration of initial NCs in both reactions was optimized to produce the dimer morphology. The statistical analyses of the product in Figure 3d revealed a non-Poissonian distribution of cluster sizes with two-particle assemblies accounting for 55% of all nanocomposites (Figure SF12a). The yield of dimer-type assemblies increases to above 90% at higher fusion temperatures (Fig. SF13d). On the other hand, increasing the concentration of nanoparticles in the reaction mixture produced larger particle clusters (n >2), as shown in Figure 3f.

According to TEM images of fused CdX (X = S, Se) NCs in Figures 3d-3f, the geometry of nanoparticles changes from zero- to quasi one-dimensional. This trend is evident through characteristic changes in absorption profiles of both NC types (Figures 3a and 3b). Upon the formation of dimer structures, the lowest-energy exciton feature red-shifts, meanwhile the dipole strength of higher energy absorbing transitions increases (resulting in a shoulder-like absorbance). Both of these changes are representative features of an exciton fine structure transitioning from a zero- to a one-dimensional character. As illustrated in Figure 3g, eight lowest-energy exciton states in CdSe NCs are expected to shift lower in energy and reorder when two dots are fused into an ellipsoid of the same diameter.[49,50] In spherical CdSe NCs, the upper $F_{bright} = \pm 1$ states (F = S + J is the total angular momentum) carry most of the dipole strength for optical absorption, while the lower $F_{bright} = \pm 1$ states are responsible for the room-temperature emission. When CdSe is elongated along the wurtzite *c*-axis, the upper $F = \pm 1_{bright}$ states drop in energy (up to 80 meV, depending on the diameter and aspect ratio of a nanorod).[51] In the case of dimer-like structures, we expect that the decrease in the upper $F = \pm 1_{bright}$ state energy will result in the upper and lower $F = \pm 1_{bright}$ states to become near-degenerate,[51] causing a red-shift of the absorbance edge, as was observed in Figures 3a and 3b. Furthermore, upon elongation of a CdSe NC, $F = 0_{bright}$ states gain additional dipole strength compared to a spherical geometry, which is expected to broaden the emission in

CdSe dimers (since F = 0_{bright} are now included in the emission along with F = ±1, and all states are thermally populated). According to Figure 3b, a ~18% PL broadening was indeed observed upon CdSe NC dimer formation. The enhancement of the F = 0_{bright} dipole strength also shortens the radiative lifetime of an exciton,[50] which could explain the reduced PL lifetime in fused CdSe nanostructures (Figure 3c).

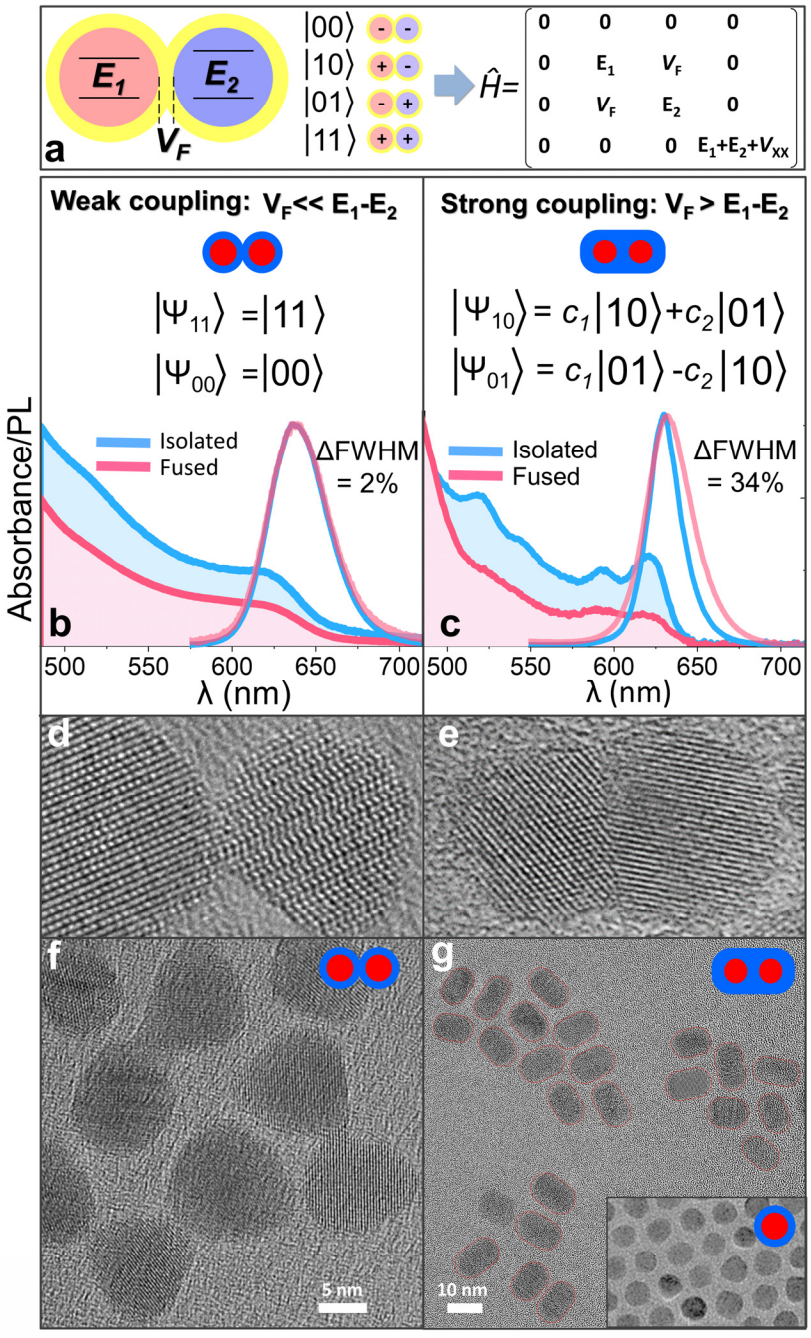

Figure 4. (a). Schematic representation of excitonic states in a hetero-dimers. E_1 and E_2 are the exciton energies in each nanoparticle (E_1<E_2). The coupling terms V_F and V_{XX} are the Förster (transition dipole-dipole) and biexciton (static dipole-dipole) interaction strengths, respectively. (b). Emission and

absorption profiles of a monomer (blue) and a weakly-coupled hetero-dimer (red) morphologies of CdSe/CdS core/shell NCs. (c). Emission and absorption profiles of a monomer (blue) and a strongly-coupled hetero-dimer (red) morphologies of CdSe/CdS core/shell NCs. (d,f). TEM images of weakly-coupled CdSe/CdS core/shell NCs, fabricated using the FA fusion strategy at T = 130 °C. (e, g). TEM images of strongly-coupled CdSe/CdS core/shell NCs, fabricated using the OLAM-S fusion strategy at T = 180 °C.

In contrast to homogenous nanocrystal molecules (CdS-CdS, CdSe-CdSe), where electronic states delocalizes over the entire structure, assemblies of CdSe/CdS core/shell NCs could lead to an adjustable coupling of single-particle exciton states. Recent work on the direct attachment of CdSe/CdS core/shell NCs[37] has provided evidence of exciton delocalization across the two CdSe domains separated by the barrier of the CdS shell. Therefore, coupled CdSe/CdS NC molecules could support a superposition of low-energy excitonic states, which are mixed by Coulomb exchange (Förster) interaction.

In assemblies of CdSe/CdS NCs, the superposition of excitonic states could be expressed using a single-particle basis set of 4 states corresponding to exciton being present (1) or absent (0) on each dot (Figure 4a). Previously, theoretical models of electronic states in a two-particle dimer considered the direct Coulomb binding energy between two excitons (V_{XX}).[19,37] In this work, we take into account both the direct Coulomb energy V_{XX} (a diagonal term of the H-matrix) and the Coulomb exchange (Förster) interaction, which is off-diagonal and therefore induces the transfer of an exciton from one QD to the other. Using this nomenclature, we can define the four states of a NC hetero-dimer as $|00\rangle, |10\rangle, |01\rangle, |11\rangle$, with the first digit referring to dot 1 and the second to dot 2. If Förster interaction, V_F, is comparable or greater than the difference between exciton energies in each dots ($V_F \geq \Delta E = E_1 - E_2$), single-particle states $|10\rangle, |01\rangle$ become strongly coupled and are no longer eigenfunctions of the system.[52] This can be verified by examining the system Hamiltonian[53] in Figure 4a. If coupling is weak, $V_F/\Delta E << 1$, the eigenstates are $|10\rangle$, $|01\rangle$. However, if the Förster interaction is strong, $V_F/\Delta E \geq 1$, eigenstates will become the superposition of single-particle states $|00\rangle$, $c_1|10\rangle + c_2|01\rangle$, $c_1|01\rangle - c_2|10\rangle, |11\rangle$ (where c_1 and c_2 are given by Eq. SE2). Consequently, the system excited at dot 1, would naturally evolve into a superposition of single-particle excitonic states $|10\rangle$, $|01\rangle$, under the action of the time–evolution operator, $\Psi(t) = \exp\left(-i\hat{H}t/\eta\right)|10\rangle$. In analogy to coupled epitaxial quantum dots,[54] such a pair of interacting

colloidal CdSe/CdS NCs can therefore represent the simplest two-level exciton system (qubit) in quantum computing applications.

In this work, we demonstrate both weak and strong coupling regimes of exciton states in CdSe/CdS NC hetero-dimers. The term hetero-dimers was originally defined[37] as same-type core-shell NCs fused at heteronymous faces (heteroplane attachment of same-type particles). Following this terminology, we refer to hetero-dimers as assemblies of same-type particles, which attach predominantly at heteronymous faces (see Figure S14). Weakly coupled hetero-dimers were fabricated by using the FA fusion strategy at T = 130 °C (method 2 in Exp. Section), which resulted in the interfacial fusion of CdS shell components (Figures 4d, 4f). Both absorbance and PL spectral features of fused nanocrystals did not change significantly from those of isolated NCs (Fig. 4b), suggesting that excitons were well localized in individual dots. To obtain strongly-coupled hetero-dimers, the fusion reaction was performed by the injection of S in the OLAM solution of CdSe/CdS NCs at T = 180 °C. The use of elevated temperatures has allowed bringing the two CdSe core domains into a closer proximity. According to TEM images in Figures 4e and 4g the starting, spherical core/shell NCs (insert in Figure 4g) were combined to form oval-shaped hetero-dimers. These structures exhibited a strong interaction of single-particle excitonic states, which was evidenced through emission changes. Broadening of the emission in hetero-dimers (accompanied by a small re-shift) is consistent with the fact that eigenvalues of the two superposition states are both lower in energy than that of a monomer, $E_{i=1,2} = E_{monomer} - 0.5\Delta E_{monomer}\left(1 \pm \sqrt{1+4\left(V_F/\Delta E_{monomer}\right)^2}\right)$. By comparing the PL of QDs before and after fusion, we extract the strength of Förster interaction, $V_F \approx 12$ meV. Based on these observations, we conclude that strongly-coupled CdSe/CdS NC hetero-dimers exhibit a superposition of single-particle excitonic states. We also expect that coupling of a greater number of CdSe/CdS NCs (Figure 5e) could extend mixing of exciton states beyond nearest neighbors.

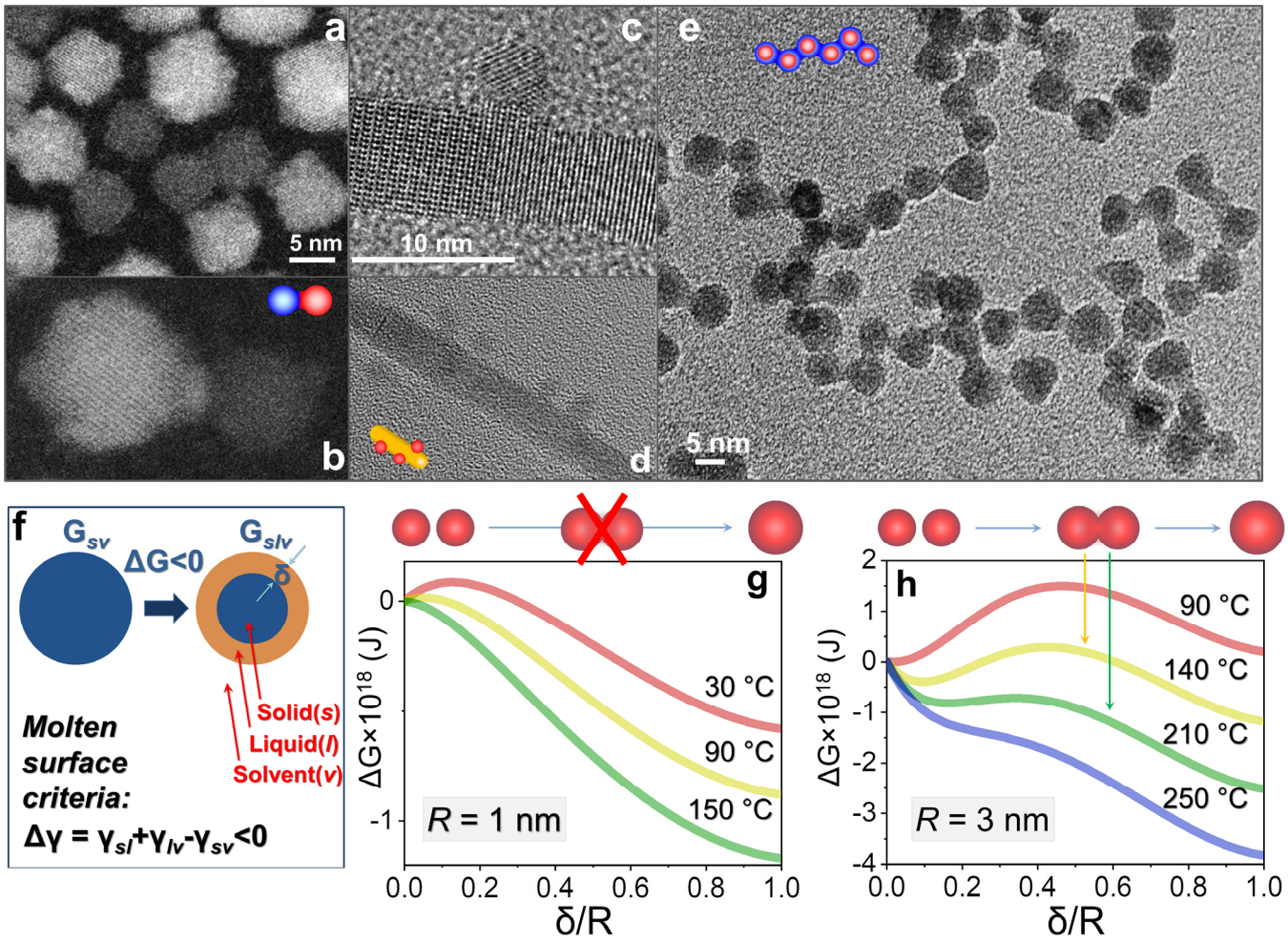

Figure 5.(a,b). High angle annular dark field (HAADF)-STEM imaging of CdS-PbS assemblies comprising 8.6-nm PbS (lighter shade) and 6.1-nm CdS (darker shade) nanocrystals. (c-d). TEM images of nanocrystal assemblies comprising CdS NCs attached to CdS nanorods. (e). Chain-like assemblies of CdSe/CdS core/shell NCs. (f). A thermodynamic model of surface melting in spherical nanocrystals. The reduction in the nanoparticle free energy (ΔG) drives the formation of the molten layer with the thickness δ. Melting is observed if the solid/solvent interfacial tension (γ_{SV}) is reduced upon the insertion of a liquid layer: $\gamma_{SL} + \gamma_{LV} - \gamma_{SV} < 0$, where γ_{SL} and γ_{LV} are the solid/liquid and liquid/solvent interfacial tensions, respectively. (g,h). The dependence of the free energy change, ΔG, on the molten layer width, δ, for CdSe NCs at different solvent temperatures. Parameters of calculation are provided in Sec. SI.4. For small size CdSe NCs (R=1 nm), shown in (g), the global minimum of ΔG at $\delta/R \rightarrow 1$ suggests melting of the entire nanoparticle (no surface melting), whereas in (h) for larger CdSe NCs (R = 3 nm), a molten layer is energetically favorable across a temperature range (e.g. at T = 140 °C and T = 210 °C).

The fusion-assembly approach was also used to achieve hetero-epitaxial bonds between dissimilar semiconductor materials. This was demonstrated through the assembly of rock-salt PbS and wurtzite CdS NCs. According to the TEM image of the reaction product in Figures 5a and 5b, heterogeneous assemblies

of CdS and PbS NCs were formed on par with homogenous clusters (CdS-CdS and PbS-PbS), accounting for at least 15% of morphologies (see Figure S5b for the statistical analysis). The interface of CdS and PbS domains appeared to have minimal alloying despite the difference in the type of the two lattice structures. We speculate that molten surfaces of fusing nanoparticles help alleviating the heteroepitaxial strain through the formation of an ion-diffusion boundary.[55] Similar domain interfaces were also observed at interfaces of CdS nanorods and CdS QDs, shown in Figures 5c,5d. The above examples of the hetero-epitaxial fusion suggests that a utilization of molten surfaces in colloidal inorganic NCs could be a feasible strategy for coupling lattice-mismatched materials.

Controlling the process of nanoparticle fusion during assembly requires understanding of molten layer formation in semiconductor colloids. Thermodynamically,[41,56,57] melting of the surface layer in inorganic nanoparticles is caused by the reduction of the interfacial energy between the solid (nanoparticle) and matrix (either solvent/ligand or vacuum) phases. This concept is illustrated in Figure 5f, indicating that the reduction of free energy, $\Delta G < 0$, is caused by the reduction in the nanoparticle interfacial tension (γ_{SV}) upon melting of the surface layer, such that $\gamma_{SL} + \gamma_{LV} - \gamma_{SV} < 0$, where γ_{SL} and γ_{LV} are the solid-liquid and liquid-solvent tension terms. Consequently, the formation of a molten (liquid) layer represents a general property of the inorganic phase, as was evident from early studies on bulk surfaces[58] (Figure S10).

In case of small-diameter nanoparticles, the onset of surface melting due to interfacial tension is contributed both by solid/solvent interactions and by the curvature of a particle (see Sec. SI.4 and Figure S11). The corresponding change in the free energy with increasing liquid layer thickness, δ, $\Delta G(\delta) = G_{slv} - G_{sv}$, was calculated in this work by adapting the Kofman approximation[56] to spherical nanoparticles in solution (Sec. SI.4). The minimum of $\Delta G(\delta, T)$ at each temperature provides the expected thickness of the molten layer, $\delta(T)$, as illustrated in the case of R=3 nm CdSe NCs in Figure 5h. At T = 90 °C, ΔG is positive for any δ, indicating that melting does not occur. At T = 140 °C, ΔG exhibits a minimum at δ/R = 0.1 (0.3 nm), which implies that surface melting is energetically favorable at this temperature. The thickness of the molten layer increases to δ/R = 0.18 (0.54 nm) at T = 210 °C, which is consistent with the TEM image of partly fused nanocrystal assemblies in Figures 1 and 2. At T = 250 °C, the global minimum of ΔG occurs at $\delta/R \rightarrow 1$, indicating that the entire particle becomes molten. Fusion of these nanoparticles results in their full coalescence as can be verified by the TEM image of the reaction product at these temperatures (Figure 1, rightmost frame). In case of small-size CdSe NCs (R = 1 nm), no local minimum of ΔG is observed (Figure 5g). Instead, increasing the temperature to above 90 °C results in a global

minimum at $\delta/R \rightarrow 1$, indicating that the entire particle becomes molten. These predictions agree with the experimental data on fusion of small-diameter CdSe NCs (Figure S12) showing a sharp transition from isolated particles to nearly coalesced dimers when the temperature is increased from 120 °C to 140 °C.

Overall, the above model predictions indicate that the onset of surface melting in semiconductor nanocrystals occurs at a relatively low thermal threshold, which agrees with experimental observation of nanocrystal fusion at these temperatures. Consequently, ripening processes of nanoparticles growth that benefit from a molten layer formation, such as digestive or Ostwald ripening, would be strongly enhanced under these conditions and should be considered when modelling colloidal growth reactions.

In summary, we have demonstrated a colloidal strategy for building coupled assemblies of semiconductor nanocrystals. The present approach exploits a general property of inorganic colloids to form a molten surface layer upon heating, which allows attaching nanoparticles at hybrid interfaces. The assembly method was demonstrated through the synthesis of homogenous (CdS-CdS, CdSe-CdSe, PbS-PbS) and heterogeneous (CdS-PbS, CdS-CdSe, CdSe/CdS-CdSe/CdS) nanocrystal molecules, where the interaction between assembly components was mediated by charge and energy transfer processes. Hetero-dimer assemblies of CdSe/CdSe NCs exhibited evidence of the exciton band formation with a tunable superposition of single-particle states. The dynamics of nanoparticle assembly was successfully explained within the viscoelastic interaction theory developed for molten-surface colloids. Predictions of this model were found in a good agreement with the experimentally observed formation of nanocrystal molecules and alloyed interfaces. Such molten-particle interactions could be relevant for many synthetic processes, including aggregative growth, oriented attachment, and coalescence. Overall, we expect that the demonstrated molten-surface assembly of semiconductor nanocrystals will provide a synthetic and theoretical foundation needed for building artificial molecules of potentially many inorganic nanocrystals.

Acknowledgment. This work was supported by the Award DE-SC0016872 (MZ) funded by the U.S. Department of Energy, Office of Science. The authors acknowledge the financial support of the University of Michigan College of Engineering and NSF grant #DMR-9871177, and technical support from the Michigan Center for Materials Characterization.

Supporting information. Additional figures, including TEM images and PL spectra. Experimental procedures and synthetic details section. Model calculations of total energy of fusing nanoparticles. Theoretical description of surface melting in colloidal inorganic nanocrystals.

REFERENCES

[1] Katz, E.; Willner, I. Integrated Nanoparticle-Biomolecule Hybrid Systems: Synthesis, Properties, and Applications. *Angew. Chem. Int. Ed.* **2004**, *43*, 6042-6108.

[2] Kagan, C. R.; Lifshitz, E.; Sargent, E. H.; Talapin, D. V. Building devices from colloidal quantum dots. *Science*. **2016**, *353*, 885.

[3] Kovalenko, M. V; Manna, L.; Cabot, A.; Hens, Z.; Talapin, D. V.; Kagan, C. R.; Klimov, V. I.; Rogach, A. L.; Reiss, P.; Milliron, D. J.; Guyot-Sionnnest, P.; Konstantatos, G.; Parak, W. J.; Hyeon, T.; Korgel, B. A.; Murray, C. B.; Heiss, W. Prospects of Nanoscience with Nanocrystals. *ACS Nano.* **2015**, *9*, 1012–1057.

[4] Gilroy, K. D.; Ruditskiy, A.; Peng, H. C.; Qin, D.; Xia, Y. Bimetallic Nanocrystals: Syntheses, Properties, and Applications. *Chem. Rev*. **2016**, *116*, 10414-10472.

[5] Wang, X.; Valiev, R. R.; Ohulchanskyy, T. Y.; Ågren, H.; Yanga, C.; Chen, G. Dye-sensitized lanthanide-doped upconversion nanoparticles. *Chem. Soc. Rev*. **2017**, *46*, 4150-4167.

[6] Kagan, C. R.; Bassett, L. C.; Murray, C. B.; Thompson, S. M. Colloidal Quantum Dots as Platforms for Quantum Information Science. *Chem. Rev*. **2021**, *121*, 3186-3233.

[7] Kroupa, D. M.; Pach, G. F.; Vörös, M.; Giberti, F.; Chernomordik, B. D.; Crisp, R. W.; Nozik, A. J.; Johnson, J. C.; Singh, R.; Klimov, V. I.; Galli, G.; Beard, M. C. Enhanced Multiple Exciton Generation in PbS|CdS Janus-like Heterostructured Nanocrystals. *ACS Nano*. **2018**, *12*, 10084–10094.

[8] Danek, M.; Jensen, K. F.; Murray, C. B.; Bawendi, M. G. Synthesis of Luminescent Thin-Film CdSe/ZnSe Quantum Dot Composites Using CdSe Quantum Dots Passivated with an Overlayer of ZnSe. *Chem. Mater*. **1996**, *8*, 173-180.

[9] Hines, M. A.; Guyot-Sionnest, P. Synthesis and Characterization of Strongly Luminescing ZnS-Capped CdSe Nanocrystals. *J. Phys. Chem.* **1996**, *100*, 468–471.

[10] Peng, X.; Schlamp, M. C.; Kadavanich, A. V.; Alivisatos, A. P. Epitaxial Growth of Highly Luminescent CdSe/CdS Core/Shell Nanocrystals with Photostability and Electronic Accessibility. *J. Am. Chem. Soc*. **1997**, *119*, 7019−7029.

[11] Zhang, J.; Chernomordik, B. D.; Crisp, R. W.; Kroupa, D. M.; Luther, J. M.; Miller, E. M.; Gao, J.; Beard, M. C. Preparation of Cd/Pb Chalcogenide Heterostructured Janus Particles via Controllable Cation Exchange. *ACS Nano*. **2015**, *9*, 7151−7163.

[12] Shao, Q.; Wang, P.; Huang, X. Opportunities and Challenges of Interface Engineering in Bimetallic Nanostructure for Enhanced Electrocatalysis. *Adv. Funct. Mater*. **2019**, *29*, 1806419.

[13] Carbone, L.; Nobile, C.; Giorgi, M. D.; Sala, F. D.; Morello, G.; Pompa, P.; Hytch, M.; Snoeck, E.; Fiore, A.; Franchini, I. R.; Nadasan, M.; Silvestre, A. F.; Chiodo, L.; Kudera, S.; Cingolani, R.; Krahne, R.; Manna, L. Synthesis and Micrometer-Scale Assembly of Colloidal CdSe/CdS Nanorods Prepared by a Seeded Growth Approach. *Nano Lett*. **2007**, *7*, 2942–2950.

[14] Hewa-Kasakarage, N. N.; Kirsanova, M.; Nemchinov, A.; Schmall, N.; El-Khoury, P. Z.; Tarnovsky, A. N.; Zamkov, M. Radiative recombination of spatially extended excitons in (ZnSe/CdS)/CdS heterostructured nanorods. *J. Am. Chem. Soc*. **2009**, *131*, 1328–1334.

[15] Shieh, F.; Saunders, A. E.; Korgel, B. A. General Shape Control of Colloidal CdS, CdSe, CdTe Quantum Rods and Quantum Rod Heterostructures. *J. Phys.Chem. B*. **2005**, *109*, 8538-8542.

[16] Halpert, J. E.; Porter, V. J.; Zimmer, J. P.; Bawendi, M. G. Synthesis of CdSe/CdTe Nanobarbells. *J. Am. Chem. Soc*. **2006**, *128*, 12590-12591.

[17] Kudera, S.; Carbone, L.; Casula, M. F.; Cingolani, R.; Falqui, A.; Snoeck, E.; Parak, W. J.; Manna, L. Selective Growth of PbSe on One or Both Tips of Colloidal Semiconductor Nanorods. *Nano Lett*. **2005**, *5*, 445-449.

[18] Carbone, L.; Cozzoli, P. D. Colloidal heterostructured nanocrystals: Synthesis and growth mechanisms. *Nanotoday*. **2010**, *5*, 449-493.

[19] Pedetti, S.; Ithurria, S.; Heuclin, H.; Patriarche, G.; Dubertret, B. Type-II CdSe/CdTe Core/Crown Semiconductor Nanoplatelets. J. Am. Chem. Soc. 2014, 136, 16430-16438.

[20] Amirav, L.; Alivisatos, P. A. J. Photocatalytic Hydrogen Production with Tunable Nanorod Heterostructures. *Phys. Chem. Lett*. **2010**, *1*, 1051–1054.

[21] Acharya, K. P.; Khnayzer, R. S.; O'Connor, T.; Diederich, G.; Kirsanova, M.; Klinkova, A.; Roth, D.; Kinder, E.; Imboden, M.; Zamkov, M. The role of hole localization in sacrificial hydrogen production by semiconductor-metal heterostructured nanocrystals. *Nano Lett*. **2011**, *11*, 2919–2926.

[22] Zhu, H.; Song, N.; Lv, H.; Hill, C. L.; Lian, T. Near unity quantum yield of light-driven redox mediator reduction and efficient H2 generation using colloidal nanorod heterostructures. *J. Am. Chem. Soc*. **2012**, *134*, 11701–11708.

[23] Shirasaki, Y.; Supran, G. J.; Bawendi, M. G.; Bulovic, V. Emergence of Colloidal Quantum-Dot LightEmitting Technologies. *Nat. Photonics***. 2013**, *7*, 13–23.

[24] Shen, H.; Gao, Q.; Zhang, Y.; Lin, Y.; Lin, Q.; Li, Z.; Chen, L.; Zeng, Z.; Li, X.; Jia, Y.; Wang, S.; Du, Z.; Li, L. S.; Zhang, Z. Visible quantum dot light-emitting diodes with simultaneous high brightness and efficiency. *Nature Photonics*. **2019**, *13*, 192–197.

[25] Jones, M. R.; Osberg, K. D.; MacFarlane, R. J.; Langille, M. R.; Mirkin, C. A. Templated Techniques for the Synthesis and Assembly of Plasmonic Nanostructures. *Chem. Rev.* **2011**, *111*, 3736−3827.

[26] Yi, C.; Liu, H.; Zhang, S.; Yang, Y.; Zhang, Y.; Lu, Z.; Kumacheva, E.; Nie, Z. Self-limiting Directional Nanoparticle Bonding Governed by Reaction Stoichiometry. *Science*. **2020**, *369*, 1369–1374.

[27] Seeman, N. C. DNA in a Material World. *Nature*. **2003**, *421*, 427-431.

[28] Zheng, J.; Constantinou, P. E.; Micheel, C.; Alivisatos, A. P.; Kiehl, R. A.; Seeman, N. C. Two-Dimensional Nanoparticle Arrays Show the Organizational Power of Robust DNA Motifs. *Nano Lett*. **2006**, *6*, 1502-1504.

[29] Jones, M. R.; Seeman, N. C.; Mirkin, C. A. Nanomaterials. Programmable Materials and the Nature of the DNA Bond. *Science.* **2015***, 347*, 1260901.

[30] Prodan, E.; Radloff, C.; Halas, N. J.; Nordlander, P. A Hybridization Model for the Plasmon Response of Complex Nanostructures. *Science*. **2003**, *302*, 419-422.

[31] Kim, J. Y.; Kotov, N. A. Charge Transport Dilemma of Solution-Processed Nanomaterials. *Chem. Mater*. **2013**, *26*, 134-152.

[32] Song, L.; Deng, Z. X. Valency Control and Functional Synergy in DNA-Bonded Nanomolecules. *ChemNanoMat.* **2017***, 3*, 698-712.

[33] Xu, X.; Stöttinger, S.; Battagliarin, G.; Hinze, G.; Mugnaioli, E.; Li, C.; Müllen, K.; Basché, T. Assembly and Separation of Semiconductor Quantum Dot Dimers and Trimers. *J. Am. Chem. Soc*. **2011**, *133*, 18062–18065.

[34] Salzmann, B. B. V.; van der Sluijs, M. M.; Soligno, G.; Vanmaekelbergh, D. Oriented Attachment: From Natural Crystal Growth to a Materials Engineering Tool. *Acc. Chem. Res*. **2021,** *54*, 787-797.

[35] Koley, S.; Cui, J.; Panfil, Y. E.; Banin, U.. Coupled Colloidal Quantum Dot Molecules. *Accounts of Chemical Research*, **2021**, *54*, 1178-1188.

[36] Hu, Y.; Sun, Y. A Generic Approach for the Synthesis of Dimer Nanoclusters and Asymmetric Nanoassemblies. *J. Am. Chem. Soc*. **2013**, *135*, 2213-2221.

[37] Cui, J.; Panfil, Y. E.; Koley, S.; Shamalia, D.; Waiskopf, N.; Remennik, S.; Popov, I.; Oded, M.; Banin, U. Colloidal Quantum Dot Molecules Manifesting Quantum Coupling at Room Temperature. *Nat. Commun*. **2019**, *10*, 5401.

[38] Cui, J.; Koley, S.; Panfil, Y. E.; Levi, A.; Waiskopf, N.; Remennik, S.; Oded, M.; Banin, U. Semiconductor Bow-Tie Nanoantenna from Coupled Colloidal Quantum Dot Molecules. *Angew. Chem. Int. Edit.* **2021**, *60*, 14467-14472.

[39] Goodman, B. M.; Somorjai, G. A. Low-Energy Electron Diffraction Studies of Surface Melting and Freezing of Lead, Bismuth, and Tin Single-Crystal Surfaces. *J. Chem. Phys*. **1970**, *52*, 6325.

[40] Wang, Z. L.; Petroski, J. M.; Green, T. C.; El-Sayed, M. A. Shape Transformation and Surface Melting of Cubic and Tetrahedral Platinum Nanocrystals*. J. Phys. Chem. B.* **1998***, 102*, 32.

[41] Buffat, Ph.; Borel, J. P. Size effect on the melting temperature of gold particles. *Phys. Rev. A*. **1976**, *13*, 2287.

[42] Goldstein, A. N.; Echer, C. M.; Alivisatos, A. P. Melting in Semiconductor Nanocrystals. *Science*. **1992**, *256*, 1425-1427.

[43] Razgoniaeva, N.; Yang, M.; Garrett, P.; Kholmicheva, N.; Moroz, P.; Eckard, H.; Romero, L. R.; Porotnikov, D.; Khon, D.; Zamkov, M. Just Add Ligands: Self-Sustained Size Focusing of Colloidal Semiconductor Nanocrystals*. Chem. Mater*. **2018**, *30*, 1391-1398.

[44] Cassidy, J.; Ellison, C.; Bettinger, J.; Yang, M.; Moroz, P.; Zamkov, M. Enabling Narrow Emission Linewidths in Colloidal Nanocrystals through Coalescence Growth. *Chem. Mater*. **2020**, *32*, 7524-7534.

[45] Pawar, A. B.; Caggioni, M.; Hartel, R. W.; Spicer, P. T. Arrested coalescence of viscoelastic droplets with internal microstructure. *Faraday Discuss,* **2012***, 158*, 341-350.

[46] Owen, J. S.; Park, J.; Trudeau, P. E.; Alivisatos, A. P. Reaction Chemistry and Ligand Exchange at Cadmium−Selenide Nanocrystal Surfaces. *J. Am. Chem. Soc*. **2008**, *130*, 12279−12281.

[47] Scholes, G. D. Controlling the optical properties of inorganic nanoparticles. *Adv. Funct. Mater.* **2008***, 18*, 1157-1172.

[48] Kholmicheva, N.; Yang, M.; Moroz, P.; Eckard, H.; Vore, A.; Cassidy, J.; Pushina, M.; Boddy, A.; Porotnikov, D.; Anzenbacher, P.; Zamkov, M. Ion-Mediated Ligand Exchange and Size Focusing of Semiconductor Nanocrystals in Ligand-Saturated Solutions. *J. Phys. Chem. C*. **2018**, *122*, 23623-23630.

[49] Scholes, G. D.; Kim, J.; Wong, C. Y.; Huxter, V. M.; Nair, P. S.; Fritz, K. P.; Kumar, S. Nanocrystal shape and the mechanism of exciton spin relaxation. *Nano Lett.* **2006***, 6*, 1765-1771.

[50] Shabaev, A.; Efros, A. L. 1D exciton spectroscopy of semiconductor nanorods. *Nano Lett.* **2004***, 4*, 1821-1825.

[51] Zhao, Q.; Graf, P. A.; Jones, W. B.; Franceschetti, A.; Li, J.; Wang, L.; Kim, K. Shape dependence of band-edge Exciton fine structure in CdSe nanocrystals. *Nano Lett.* **2007***, 7*, 3274-3280.

[52] Chen, T.; Reich, K. V.; Kramer, N. J.; Fu, H.; Kortshagen, U. R.; Shklovskii, B. I. Metal-Insulator Transition in Films of Doped Semiconductor Nanocrystals. *Nat. Mater.* **2016**, *15*, 299– 303.

[53] Lovett, B. W.; Reina, J. H.; Nazir, A.; Briggs, G. Optical schemes for quantum computation in quantum dot molecules. *Phys. Rev. B* **2003***, 68*, 205319.

[54] Schedelbeck, G.; Wegscheider, W.; Bichler, M.; Abstreiter, G. Coupled quantum dots fabricated by cleaved edge overgrowth: from artificial atoms to molecules. *Science*. **1997**, *278*, 1792–1795.

[55] Grossmann, A.; Erley, W.; Hannon, J. B.; Ibach, H. Giant Surface Stress in Heteroepitaxial Films: Invalidation of a Classical Rule in Epitaxy. *Phys Rev Lett***. 1996**, *77*, 127-130.

[56] Kofman, R.; Cheyssac, P.; Aouaj, A.; Lereah, Y.; Deutscher, G.; Ben-David, T.; Penisson, J. M.; Bourret, A. Surface melting enhanced by curvature effects. *Surface Science*. **1994**, *303*, 231-246.

[57] Mei, Q. S.; Lu, K. Melting and superheating of crystalline solids: From bulk to nanocrystals. *Progress in Materials Science*. **2007**, *52*, 1175–1262.

[58] van der Veen, J. F. Melting and freezing at surfaces. *Surf Sci.* **1999***, 433-435*, 1-11.